International Journal of Automotive Technology, Vol. 19, No. 1, pp. 63−75 (2018)
DOI 10.1007/s12239−018−0007−2

pISSN 1229−9138/ eISSN 1976−3832

TIRE WEAR ESTIMATION BASED ON NONLINEAR LATERAL DYNAMIC OF MULTI-AXLE STEERING VEHICLE

Xiang Chen, Nan Xu* and Konghui Guo

State Key Laboratory of Automotive Simulation and Control, Jilin University, Changchun, Jilin 130022, China

(Received 20 March 2017; Revised 30 June 2017; Accepted 11 July 2017)

ABSTRACT−This paper presents a novel nonlinear dynamic model of a multi-axle steering vehicle to estimate the lateral wear amount of tires. Firstly, a 3DOF nonlinear vehicle dynamic model is developed, including dynamic models of the hydro-pneumatic suspension, tire, steering system and toe angle. The tire lateral wear model is then built and integrated into the developed vehicle model. Based on the comparison of experimental and simulation results, the nonlinear model is proved to be better than a linear model for the tire wear calculation. In addition, the effects of different initial toe angles on tire wear are analyzed. As simulation results shown, the impact of the dynamic toe angle on the tire wear is significant. The tire wear amount will be much larger than that caused by normal wear if the initial toe angle increases to 1° - 1.5°. The results also suggest that the proposed nonlinear model is of great importance in the design and optimazation of vehicle parameters in order to reduce the tire wear.

KEY WORDS : Tire wear, Multi-axle steering vehicle, Nonlinear model, Lateral dynamic, Toe angle

NOMENCLATURE

m_b : vehicle body mass
m_i : vehicle unsprung mass of *i*th axle
I_{11} : moment of vehicle body inertia about X-axis
I_{33} : moment of vehicle body inertia about Z-axis
I_{13} : product of vehicle body inertia about XZ plane
I_{zzi} : moment of inertia about Z-axis (unsprung mass of *i*th axle)
X_i : signed distance from i th axle to CG (the center of gravity)
h_b : distance from roll center to sprung CG
h_{ao} : height of the roll center
h_{ai} : height of the roll center at *i*th axle
Δ : distance from mass center to steering center
B_w : vehicle wheelspan
B_K : distance around two springs of the same axle
B_C : distance around two dampers of the same axle
R_0 : free radius of the tire
R_{iL} : load radius of the left tire of *i*th axle
R_{iR} : load radius of the right tire of *i*th axle
k_z : vertical stiffness of the tire
K_i : cornering stiffness of *i*th axle tire
F_s : force of the hydro-pneumatic spring
k_s : stiffness of the hydro-pneumatic spring
C_{eq} : equivalent damping of the hydro-pneumatic spring
K_ϕ : vehicle body roll stiffness
C_ϕ : vehicle body roll damping
K_{iL} : stiffness of the left hydro-pneumatic spring of *i*th axle
K_{iR} : stiffness of the right hydro-pneumatic spring of *i*th axle
C_{iL} : damping of the left hydro-pneumatic spring of *i*th axle
C_{iR} : damping of the right hydro-pneumatic spring of *i*th axle
E_i : wheel roll steer angle per unit roll angle
u : vehicle longtitude velocity
δ_i : steering angle of *i*th axle
δ_{iL} : steering angle of left tire of *i*th axle
δ_{iR} : steering angle of right tire of *i*th axle
α_i : sideslip angle of *i*th axle
α_{iL} : sideslip angle of left tire of *i*th axle
α_{iR} : sideslip angle of right tire of *i*th axle
γ_{iL} : toe angle of left tire of *i*th axle
γ_{iR} : toe angle of right tire of *i*th axle
v : vehicle lateral velocity
ψ : vehicle yaw angle
r : vehicle yaw rate
ϕ : vehicle roll angle
β : sideslip angle of CG
v_i : lateral velocity of *i*th axle
E_T : kinetic energy of the vehicle
E_V : potential energy of the vehicle
E_{Ti} : kinetic energy of *i*th axle
E_{Tbt} : vehicle body kinetic energy of translational
E_{Tbr} : vehicle body kinetic energy of rotational
E_{Ti} : kinetic energy of *i*th axle

**Corresponding author.* e-mail: xunan@jlu.edu.cn

E_D : dissipative energy of the vehicle
F_{Qv} : lateral generalized force
F_{Qr} : yaw generalized force
$F_{Q\phi}$: roll generalized force
F_{YiL} : lateral force of left tire of ith axle
F_{YiR} : lateral force of right tire of ith axle
F_{ZiL} : vertical force of left tire of ith axle
F_{ZiR} : vertical force of right tire of ith axle
S_y : lateral slip ratio
μ_y : lateral friction coefficient
K_y : tire cornering stiffness
F_{z0} : nominal vertical load of the tire
F_z : vertical load of the tire
F_{zn} : normalized vertical load
F_y : lateral force of the tire
$\underline{\phi_y}$: normalized slip ratio
$\overline{F}_y$: normalized lateral force
E_y : curvature of the lateral force
V_{sym} : friction characteristic parameters
V_{sy} : slip speed between the road and tire
R_{wear} : wear mass per unit time and unit area
P_f : wear power per unit area
F_f : friction force
V_s : sliding speed of friction
η : proportion of the tire tread pattern
D_{patch} : width of the tire grounding mark
A_{patch} : contact area of friction
A_{patch_iL} : area of the left tire grounding of ith axle
A_{patch_iR} : area of the right tire grounding of ith axle
Δh_{iL} : wear height of left tire of ith axle
Δh_{iR} : wear height of right tire of ith axle
Δh_i : average wear height of ith axle
ρ : rubber density of the tire tread

1. INTRODUCTION

For a multi-axle vehicle, the expense caused by tire wear account for a large proportion of the operating cost (Li *et al*., 2006). In addition, the problem of tire wear will result in not only economic loss but also the environmental pollution (Huang *et al*., 2013; Lupker *et al*., 2004). The tire wear issue of a multi-axle steering vehicle tends to be crucial, with great influence on the vehicle safety, and the uneven tire wear problem is particularly serious if the alignment parameters are not reasonable. How to accurately forecast and reduce tire wear has been a hot topic (Stalnaker and Turner, 2002; Cho *et al*., 2005, 2011; Da Silva *et al*., 2012).

Till now, there have been a lot of research on tire wear. This issue is usually studied from two aspects of microcosmic wear mechanism and macroscopic vehicle dynamics.

For the microcosmic aspect, Grosch (2008) and Klüppel (2015) conducted a theoretical study on tire wear from the point view of rubber wear mechanism. Zuo *et al*. (2014) and Yang *et al*. (2016) performed a deep research on tire wear by the finite element method (FEM). Rodríguez-Tembleque *et al*. (2010, 2011) discussed the problem of rolling contact of tire wear by the boundary element method (BEM).

For the macroscopic vehicle dynamics, two approaches can be used to study this problem. They are experiment and simulation. By using the former method, Sakai (1996), Stalnaker *et al*. (1996) and Knisley (2002) established an experimental platform to simulate the outdoor driving environment. The relevant theory is provided based on their validated tire wear data.

By the latter one, Miller *et al*. (1991) and Ma *et al*. (2015) studied the problem of reducing tire wear from two aspects of optimizing Ackerman steering angle and torque distribution, respectively. Shen *et al*. (2016) decreased the wear rate of the tire by designing a hierarchical controller to determine the required yaw torque and driving force of each wheel. Da Silva *et al*. (2012) built a simplified model to study the tire wear of a multi-axle vehicle. Zhu *et al*. (2015) built a concise multi-axle vehicle dynamic model and developed a control algorithm for reducing cornering tire wear. In Zhuang (2002), the relationship between the tire wear amount and the slip ratio as well as the ground contact pressure was deduced in the case of braking and driving situation by using the brush tire model. Lupker *et al*. (2004) established a refined tire contact model, a local friction model, and a local wear model, and then put these models to a validated vehicle's multi-body model to predict the tire wear numerically.

All of the vehicle speed, tire pressure, tire load, road surface and the surrounding environment all have impact on tire wear more or less (Li *et al*., 2012). As a result, an accurate vehicle dynamic model is necessary for studying the issue of tire wear by the method of simulation. As mentioned above, previous researchers have built some models at different level of complexities to study tire wear, but to the multi-axle steering vehicle, there is still few vehicle dynamic model for studying tire wear.

In this paper, a 3DOF nonlinear dynamic model is established to study the issue of the tire wear. The proposed vehicle model accurately describes the dynamics of hydro-pneumatic suspension, tire, steering system and toe angle simultaneously. And all these factors, which are rarely modeled accurately previously for the research of multi-axle vehicle tire wear, are established nonlinearly by the experimental data. With this model, the effects of the sideslip angle, lateral force and grounding area of each tire, directly influencing tire wear, can be obtained instantaneously. Meanwhile, the experimental validation of the nonlinear vehicle model is performed. In Section 3, a local wear model is developed and the tread block test is conducted to parameterize the local wear model. Then it is integrated into the vehicle dynamic model in Section 4. In order to make the simulation condition more real, four sets of the steering angle of the first axle and vehicle velocity are collected as input to the vehicle model. In Section 5, the results of tire wear are presented quantitatively. From the experimental data and simulation results, it is obvious that the proposed nonlinear model can be used to accurately estimate the lateral tire wear amount. Moreover, the effect of different initial toe angles on tire wear is also analyzed. Finally, the conclusions are summed up in the last section.

2. VEHICLE MODEL

The suspension system, tire characteristics, steering model and wheel alignment parameters are considered when develop the vehicle model. The specific modeling process is described in the following sections.

2.1. Nonlinear 3DOF Vehicle Model

2.1.1. Coordinate system

As shown in Figure 1, the coordinate system is defined as follows (Yu and Lin, 2005), the ground coordinate system is $\boldsymbol{G}$ ($\boldsymbol{g}_1$, $\boldsymbol{g}_2$, $\boldsymbol{g}_3$), the vehicle coordinate system is $\boldsymbol{A}$ ($\boldsymbol{a}_1$, $\boldsymbol{a}_2$, $\boldsymbol{a}_3$), the vehicle body coordinate system is $\boldsymbol{B}$ ($\boldsymbol{b}_1$, $\boldsymbol{b}_2$, $\boldsymbol{b}_3$).

O_A (the center of gravity) is defined as the origin of the vehicle coordinate system $\boldsymbol{A}$. The vector $\boldsymbol{a}_1$ through the origin O_A is in the same direction with u that represents the vehicle longitudinal velocity. The vector $\boldsymbol{a}_2$ through the origin O_A is in the same direction with v that represents the vehicle lateral velocity. The vector $\boldsymbol{a}_3$ through the origin O_A is in the same direction as r that represents the vehicle yaw angle velocity. And the coordinate system $\boldsymbol{A}$ conforms to the right-hand rule.

The vehicle motion state can be represented by three variables: yaw angle ψ, sideslip angle β, roll angle ϕ. The yaw angle ψ is formed by $\boldsymbol{g}_1$ and $\boldsymbol{a}_1$, the roll angle ϕ is formed by $\boldsymbol{a}_3$ and $\boldsymbol{b}_3$. The angles of ψ and ϕ conform to the right-hand rule as well.

As Equations (1) and (2) shown, there are the following relationships of the coordinate system $\boldsymbol{G}$ and $\boldsymbol{A}$, the coordinate system $\boldsymbol{B}$ and $\boldsymbol{A}$ respectively.

$$\begin{bmatrix} \boldsymbol{g}_1 \\ \boldsymbol{g}_2 \\ \boldsymbol{g}_3 \end{bmatrix} = \begin{bmatrix} \cos\psi & -\sin\psi & 0 \\ \sin\psi & \cos\psi & 0 \\ 0 & 0 & 1 \end{bmatrix} \begin{bmatrix} \boldsymbol{a}_1 \\ \boldsymbol{a}_2 \\ \boldsymbol{a}_3 \end{bmatrix} \tag{1}$$

$$\begin{bmatrix} \boldsymbol{b}_1 \\ \boldsymbol{b}_2 \\ \boldsymbol{b}_3 \end{bmatrix} = \begin{bmatrix} 1 & 0 & 0 \\ 0 & \cos\phi & \sin\phi \\ 0 & -\sin\phi & \cos\phi \end{bmatrix} \begin{bmatrix} \boldsymbol{a}_1 \\ \boldsymbol{a}_2 \\ \boldsymbol{a}_3 \end{bmatrix} \tag{2}$$

2.1.2. Modeling illustrate

As shown in Figure 1, O_R is the steering center, H denotes the pedal of O_R to the longitudinal center line of the vehicle. Point O means the intersection of the roll center line and the plumb line through the center of gravity O_A. Ignoring the impact of the steering trapezoid, there is an approximately equal relationship: $\delta_{nL} = \delta_{nR} = \delta_n$.

The 3DOF dynamic model of multi-axle steering vehicle can be derived according to the Lagrange Equation:

$$\begin{cases} \dfrac{d}{dt}(\dfrac{\partial E_T}{\partial v}) + r\dfrac{\partial E_T}{\partial u} = F_{Qv} \\ \dfrac{d}{dt}(\dfrac{\partial E_T}{\partial r}) + u\dfrac{\partial E_T}{\partial v} - v\dfrac{\partial E_T}{\partial u} = F_{Qr} \\ \dfrac{d}{dt}(\dfrac{\partial E_T}{\partial \dot{\phi}}) - \dfrac{\partial E_T}{\partial \phi} + \dfrac{\partial E_V}{\partial \phi} + \dfrac{\partial E_D}{\partial \dot{\phi}} = F_{Q\phi} \end{cases} \tag{3}$$

where, E_T denotes the vehicle kinetic energy, E_V indicates the vehicle potential energy, E_D represents the vehicle dissipative energy, F_{Qv} means the lateral generalized force, F_{Qr} shows the yaw generalized force and $F_{Q\phi}$ is the roll generalized force.

2.1.3. Vehicle kinetic energy

Obviously, the kinetic energy of the vehicle should be divided into two parts, including the sprung mass and the unsprung mass.

(1) The kinetic energy of the unsprung part

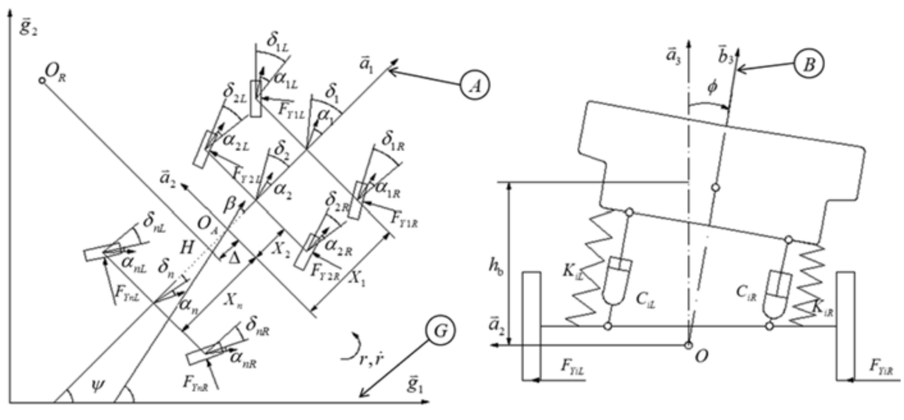

Figure 1. Nonlinear 3DOFdynamics model of multi-axle steering vehicle.

The kinetic energy of the unsprung part can be expressed as:

$$\sum E_{\mathrm{Ti}} = \sum_{\mathrm{i=1}}^{\mathrm{n}} \left(\frac{1}{2} m_{\mathrm{i}} (u_{\mathrm{i}}^2 + v_{\mathrm{i}}^2) + \frac{1}{2} I_{\mathrm{zzi}} r^2 \right) \tag{4}$$

where, $u_{\mathrm{i}} = u$, $v_{\mathrm{i}} = v + X_{\mathrm{i}} \cdot \mathrm{r}$, E_{Ti} is the kinetic energy of ith axle.

(2) The kinetic energy of sprung part

The roll angle of the sprung part will appear when the vehicle turns, and the position vector of the sprung mass center to the reference point O can be expressed as:

$$\boldsymbol{P} = h_{\mathrm{b}} \boldsymbol{b_3} = -h_{\mathrm{b}} \sin\phi \boldsymbol{a_2} + h_{\mathrm{b}} \cos\phi \boldsymbol{a_3} \tag{5}$$

The angular velocity between coordinate $\boldsymbol{B}$ and coordinate $\boldsymbol{G}$ is $\boldsymbol{\Omega}^{\mathbf{GB}}$. It can be expressed as:

$$\boldsymbol{\Omega}^{\mathbf{GB}} = \boldsymbol{\Omega}^{\mathbf{GA}} + \boldsymbol{\Omega}^{\mathbf{AB}} = \dot{\phi} \boldsymbol{b_1} + \dot{\psi} \sin\phi \boldsymbol{b_2} + \dot{\psi} \cos\phi \boldsymbol{b_3} \tag{6}$$

The velocity vector $\boldsymbol{P}$ in coordinate $\boldsymbol{G}$ can be obtained from:

$$\frac{d\boldsymbol{P}^{\mathbf{G}}}{dt} = \frac{d\boldsymbol{P}^{\mathbf{B}}}{dt} + \boldsymbol{\Omega}^{\mathbf{GB}} \times \boldsymbol{P} \tag{7}$$

However, $\frac{d\boldsymbol{P}^{\mathbf{G}}}{dt}$ can be expressed as the following form: $u_{\mathrm{b}} \boldsymbol{a_1} + v_{\mathrm{b}} \boldsymbol{a_2} + w_{\mathrm{b}} \boldsymbol{a_3}$, where:

$$\begin{cases} u_{\mathrm{b}} = u + h_{\mathrm{b}} \dot{\psi} \sin\phi \\ v_{\mathrm{b}} = v - h_{\mathrm{b}} \dot{\phi} \cos\phi \\ w_{\mathrm{b}} = -h_{\mathrm{b}} \dot{\phi} \sin\phi \end{cases} \tag{8}$$

Then the kinetic energy of translation can be acquired:

$$\begin{aligned} E_{\mathrm{Tbt}} = & \frac{1}{2} m_{\mathrm{b}} [(u + h_{\mathrm{b}} \dot{\psi} \sin\phi)^2 \\ & + (v - h_{\mathrm{b}} \dot{\phi} \cos\phi)^2 + (-h_{\mathrm{b}} \dot{\phi} \sin\phi)^2] \end{aligned} \tag{9}$$

The kinetic energy of rotation can be acquired as:

$$\begin{aligned} E_{\mathrm{Tbr}} &= \frac{1}{2} (\boldsymbol{\Omega}^{\mathbf{GB}})^{\mathbf{T}} \boldsymbol{I_{\mathrm{b}}} \boldsymbol{\Omega}^{\mathbf{GB}} \\ &= \frac{1}{2} (I_{11} \dot{\phi}^2 + I_{22} \dot{\psi}^2 \sin^2\phi + I_{33} \dot{\psi}^2 \cos^2\phi - 2 I_{13} \dot{\phi} \dot{\psi} \cos\phi) \end{aligned} \tag{10}$$

where, $\boldsymbol{I_{\mathrm{b}}}$ is the inertia vector of the sprung mass, it is a constant vector in coordinate $\boldsymbol{B}$:

$$\boldsymbol{I_{\mathrm{b}}} = \begin{bmatrix} I_{11} & -I_{12} & -I_{13} \\ -I_{21} & I_{22} & -I_{23} \\ -I_{31} & -I_{32} & I_{33} \end{bmatrix} \tag{11}$$

where, I_{ii} represents the inertia of sprung mass by the vector $\boldsymbol{b}_{\mathrm{i}}$, I_{ij} is the product of inertia of the sprung mass by the vector $\boldsymbol{b}_{\mathrm{i}}$ and $\boldsymbol{b}_{\mathrm{j}}$. The vehicle is symmetrical about the horizontal plane and longitudinal plane, so there is an approximately equal relationship: $I_{12} = I_{13} = 0$. Finally, the kinetic energy of the sprung mass can be acquired as Equation (12):

$$\begin{aligned} E_{\mathrm{T}} = & \sum_{\mathrm{i=1}}^{\mathrm{n}} (\frac{1}{2} m_{\mathrm{i}} (u_{\mathrm{i}}^2 + v_{\mathrm{i}}^2) + \frac{1}{2} I_{\mathrm{zzi}} r^2) + \frac{1}{2} m_{\mathrm{b}} [(u + h_b \dot{\psi} \sin\phi)^2 \\ & + (v - h_{\mathrm{b}} \dot{\phi} \cos\phi)^2 + (-h_{\mathrm{b}} \dot{\phi} \sin\phi)^2] \\ & + \frac{1}{2} (I_{11} \dot{\phi}^2 + I_{22} \dot{\psi}^2 \sin^2\phi + I_{33} \dot{\psi}^2 \cos^2\phi - 2 I_{13} \dot{\phi} \dot{\psi} \cos\phi) \end{aligned} \tag{12}$$

2.1.4. Vehicle potential and dissipative energy

As shown in Figure 1, the body and the chassis of the vehicle are connected by means of an elastic element and a damping element, so the potential and dissipative energy of the vehicle can be expressed as: $E_{\mathrm{V\phi}} = \frac{1}{2} K_{\phi} \phi^2$, $E_{\mathrm{D\phi}} = \frac{1}{2} C_{\phi} \dot{\phi}^2$, where K_{ϕ} and C_{ϕ} can be calculated as Equation (13):

$$\begin{cases} K_{\phi} = \frac{B_{\mathrm{K}}^2}{4} \sum_{\mathrm{i=1}}^{\mathrm{n}} (K_{\mathrm{iL}} + K_{\mathrm{iR}}) \\ C_{\phi} = \frac{B_{\mathrm{C}}^2}{4} \sum_{\mathrm{i=1}}^{\mathrm{n}} (C_{\mathrm{iL}} + C_{\mathrm{iR}}) \end{cases} \tag{13}$$

The impact on the potential energy of the sprung mass should be considered when the roll occurs. It is expressed as:

$$E_{\mathrm{Vg}} = -m_{\mathrm{b}} g h_{\mathrm{b}} (1 - \cos\phi) \tag{14}$$

Then the potential and dissipative energy can be acquired as Equation (15):

$$\begin{cases} E_{\mathrm{V}} = \frac{B_{\mathrm{K}}^2}{4} \sum_{\mathrm{i=1}}^{\mathrm{n}} (K_{\mathrm{iL}} + K_{\mathrm{iR}}) \phi^2 - m_{\mathrm{b}} g h_{\mathrm{b}} (1 - \cos\phi) \\ E_{\mathrm{D}} = \frac{B_{\mathrm{C}}^2}{4} \sum_{\mathrm{i=1}}^{\mathrm{n}} (C_{\mathrm{iL}} + C_{\mathrm{iR}}) \dot{\phi}^2 \end{cases} \tag{15}$$

2.1.5. Generalized force

According to the definition of Lagrange equation, the generalized force can be expressed as the following:

$$\begin{cases} F_{\mathrm{Qv}} = \sum_{\mathrm{i=1}}^{\mathrm{n}} (F_{\mathrm{YiL}} + F_{\mathrm{YiR}}) \\ F_{\mathrm{Qr}} = \sum_{\mathrm{i=1}}^{\mathrm{n}} (F_{\mathrm{YiL}} + F_{\mathrm{YiR}}) X_{\mathrm{i}} \\ F_{\mathrm{Q\phi}} = \sum_{\mathrm{i=1}}^{\mathrm{n}} (F_{\mathrm{YiL}} + F_{\mathrm{YiR}})(h_{\mathrm{ai}} - h_{\mathrm{ao}}) \end{cases} \tag{16}$$

2.1.6. Sideslip angle of each axis

Considering that the width of the vehicle has an impact on the sideslip angle of the left and right wheels, the difference between left and right sideslip angles is greater when the width is wider. As a result the sideslip angles of the left and right wheel are expressed respectively. The factors of roll steer and toe angle are also considered into the expressions. According to Section 2.1.2, there is an approximately equal relationship: $\delta_{\mathrm{iL}} = \delta_{\mathrm{iR}} = \delta_{\mathrm{i}}$. Then the sideslip angle of each axis can be expressed as Equation (17):

$$\begin{cases} \alpha_{iL} = \dfrac{v + X_i r}{u - \dfrac{B_w}{2} r} - \delta_i + E_i \phi + \gamma_{iL} \\ \alpha_{iR} = \dfrac{v + X_i r}{u + \dfrac{B_w}{2} r} - \delta_i + E_i \phi - \gamma_{iR} \end{cases} \tag{17}$$

where, E_i is the coefficient of roll steer, γ_{iL} and γ_{iR} are respective left and right toe angle.

2.1.7. Vertical load of each tire

When the vehicle turns, the body will produce a roll angle, resulting into a load transfer of inside and outside. This load transfer will influence the cornering force and the sideslip angle of each axle. The vertical force can be expressed as follows:

$$\begin{cases} F_{ziL} = \dfrac{1}{2} F_{zi} - \dfrac{K_{iL} B_K^2 \phi}{2B_w} - \dfrac{C_{iL} B_C^2 \dot{\phi}}{2B_w} - \dfrac{m_b h_b \ddot{\phi} R}{n B_w} \\ \qquad - \dfrac{(m_i R + m_b h_{ai}/n)(\dot{v} + ur)}{B_w} \\ F_{ziR} = \dfrac{1}{2} F_{zi} + \dfrac{K_{iR} B_K^2 \phi}{2B_w} + \dfrac{C_{iR} B_C^2 \dot{\phi}}{2B_w} + \dfrac{m_b h_b \ddot{\phi} R}{n B_w} \\ \qquad + \dfrac{(m_i R + m_b h_{ai}/n)(\dot{v} + ur)}{B_w} \end{cases} \tag{18}$$

2.1.8. Equations of the vehicle model

Overall, the equations of the Nonlinear 3DOF vehicle model can be derived as Equation (19):

$$\begin{cases} (\sum_{i=1}^{n} m_i + m_b) u \dot{\beta} + \sum_{i=1}^{n} m_i X_i \dot{r} - m_b h_b \ddot{\phi} \cos\phi + (\sum_{i=1}^{n} m_i + m_b) ur \\ + m_b h_b \dot{\phi}^2 \sin\phi + m_b h_b r^2 \sin\phi = \sum_{i=1}^{n} (F_{YiL} + F_{YiR}) \\ \sum_{i=1}^{n} m_i X_i u \dot{\beta} + [\sum_{i=1}^{n} (m_i X_i^2 + I_{zzi}) + (I_{33} \cos^2\phi + I_{22} \sin^2\phi) \\ + m_b h_b^2 \sin^2\phi] \dot{r} - I_{13} \ddot{\phi} \cos\phi + \sum_{i=1}^{n} m_i X_i ur + I_{13} \dot{\phi}^2 \sin\phi \\ + 2(m_b h_b^2 + I_{33} - I_{22}) \dot{\phi} r \sin\phi \cos\phi - m_b h_b u \beta r \sin\phi \\ = \sum_{i=1}^{n} (F_{YiL} + F_{YiR}) X_i \\ m_b h_b u \dot{\beta} \cos\phi + I_{13} \dot{r} \cos\phi - (m_b h_b^2 + I_{11}) \ddot{\phi} + m_b h_b ur \cos\phi \\ - C_\phi \dot{\phi} - K_\phi \phi + m_b g h_b \sin\phi + m_b h_b^2 \dot{\phi}^2 \sin\phi \cos\phi \\ + (m_b h_b^2 - I_{33} + I_{22}) r^2 \sin\phi \cos\phi \\ = \sum_{i=1}^{n} (F_{YiL} + F_{YiR})(h_{ao} - h_{ai}) \end{cases} \tag{19}$$

where, the sideslip angle of CG: $\beta = v/u$, and $\dot{\beta} = \dot{v}/u$.

2.2. Hydro-pneumatic Spring Test and Model

A six-axle steering terrain vehicle is carried out as thetarget vehicle. The hydro-pneumatic spring is adopted in the vehicle, which can play the role of an elastic element and a damping element. In order to obtain the precise dynamic mathematical model, the stiffness and damping characteristics of the hydro-pneumatic spring are tested. As shown in Table 1, the stiffness and damping characteristics of the hydro-pneumatic spring are simulated under the condition of low frequency and high frequency respectively.

Table 1. Hydro-pneumatic spring test condition.

Test condition	Amplitude (mm)	Frequency (Hz)	Max velocity (°)
Low frequency	50	0.05	0.0157
High frequency	50	0.54	0.1696

The process of hydro-pneumatic spring test is described as follows: first of all, an absorber test equipment is set. Then the hydro-pneumatic spring is attached onto this equipment. The two ends of the hydro-pneumatic spring are respectively arranged on the shock absorber test platform. One end of the spring is fixed on the equipment and the other end performs the reciprocating motion with the assist of an actuator of the platform. The data acquisition system will collect the force and displacement of the actuator simultaneously.

As shown in Figure 2, the stiffness characteristic curves can be obtained in the condition of low-frequency test. The relationship between the force and displacement is obtained by curve fitting:

$$\begin{aligned} F_s &= -50.1307 + 0.4912x - 4.3 \times 10^{-3} x^2 \\ &\quad + 3.2484 \times 10^{-5} x^3 \ \text{(KN)} \end{aligned} \tag{20}$$

Then the stiffness expression of the hydro-pneumatic spring can be obtained from Equation (21):

$$k_s = 0.4912 - 8.6 \times 10^{-3} x + 9.7452 \times 10^{-5} x^2 \ \text{(KN/mm)} \tag{21}$$

The damping characteristic of the hydro-pneumatic spring is obtained in the condition of high frequency test and energy method. As shown in Figure 3, the damping energy is calculated by the method of numerical integration, then the damping energy can be obtained: $\Delta E = 1.364 \times 10^4$ J, and there is a relationship in one period:

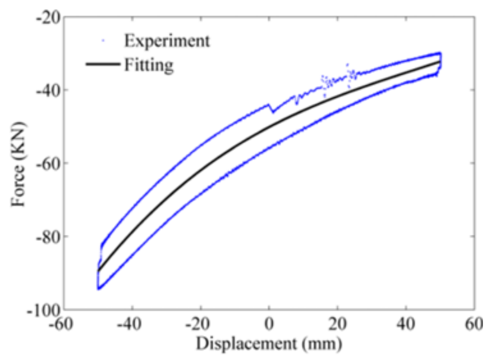

Figure 2. Stiffness characteristic curve.

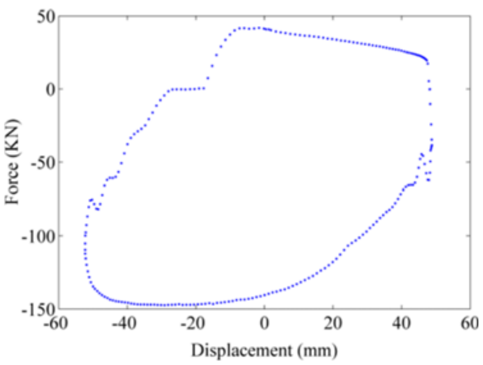

Figure 3. Damping characteristic curve.

$$\Delta E = \oint C_{eq}\dot{x}dx = \oint C_{eq}(2\pi fA)^2\cos^2(2\pi f)dx \\ = 2f(2\pi A)^2 C_{eq} \tag{22}$$

Finally, the damping coefficient can be calculated: C_{eq} = 2.9876 × 105 (N s/m)

Then the value K_{iL}, K_{iR} and C_{iL}, C_{iR} in Equation (13) can be obtained as:

$$\begin{cases} K_{iL} = K_{iR} = k_s \\ C_{iL} = C_{iR} = C_{eq} \end{cases} \tag{23}$$

2.3. Tire Model and Test

2.3.1. Tire model

As the only one component transferring the interaction force from the vehicle to the ground, the tire plays a very important role and its stress in the contact patch is very complicated. So it is very difficult to establish an analytical model that can fully describe the characteristics of the tire-road contact. Therefore, the UniTire model a semi-empirical model is used to describe the characteristics of the tire-road contact for its conciseness and precision (Guo, 2011; Xu, 2012). Here, the characteristics of the sideslip were mainly considered. Firstly, some definitions are given:

$$\phi_y = \frac{K_y S_y}{\mu_y F_z} \tag{24}$$

$$\overline{F}_y \cdot \mathrm{sgn}(\phi_y) = \frac{F_y}{\mu_y F_z} \tag{25}$$

$$F_{zn} = \frac{F_z}{F_{z0}} \tag{26}$$

where, S_y is the lateral slip ratio, μ_y is the lateral friction coefficient, K_y denotes the tire cornering stiffness, F_{z0} means the nominal vertical load of the tire, F_z is the vertical load of the tire, F_{zn} is the normalized vertical load, F_y represents the lateral force of the tire, ϕ_y indicates the normalized slip ratio, $\overline{F}_y$ shows the normalized lateral force. There is a relationship between ϕ_y and $\overline{F}_y$ shown in Equation (27):

$$\left|\overline{F}_y\right| = 1 - \exp\left[-\left|\phi_y\right| - E_y\left|\phi_y^2\right| - \left(E_y{}^2 + \frac{1}{12}\right)\left|\phi_y^3\right|\right] \tag{27}$$

where, E_y is the curvature of the lateral force, the variations E_y, K_y, S_y and μ_y can be expressed as Equations (28) ~ (31):

$$E_y = \frac{1}{2 + s_1^2\exp\left(-\frac{F_{zn}}{s_2^2}\right)} \tag{28}$$

$$K_y = \frac{F_z}{s_3^2 + s_4^2 F_{zn} + s_5^2 F_{zn}^2} \tag{29}$$

$$S_y = -\tan\alpha \tag{30}$$

$$\mu_y = \mu_{ys} + (\mu_{y0} - \mu_{ys}) \cdot \\ \exp\left(-\mu_{yh}^2\log^2\left(\left|\frac{V_{sy}}{V_{sym}}\right| + N\exp\left(-\left|\frac{V_{sy}}{V_{sym}}\right|\right)\right)\right) \tag{31}$$

where, α is the tire sideslip angle, μ_{y0}, μ_{ys}, μ_{yh} and V_{sym} are friction characteristic parameters, which can be further developed as functions of vertical load. N (usually $N = 0.8$) is a factor to make the friction coefficient increase slightly around the origin ($\left|V_{sy}\right| < V_{sym}$) and V_{sy} is the slip speed between the road and tire. s_0, s_1, s_2, s_3, s_4 and s_5 are five fitting constants.

2.3.2. Tire sideslip test and fitting

In order to obtain the fitting parameters, the tire test of pure sideslip is made, and the test process is as follows: firstly, a tire test equipment is set up, then the tire axle is fixed on the test bench but the tie tread can roll freely on the test bench. When the test begins, there is a certain angle representing the sideslip angle between the tire center plane and the movement direction of the test bench. Meanwhile, the test bench will apply the loading force to the tire as the vertical load. The data acquisition system will collect the lateral force of the test bench the same as the tire lateral force. The tire test can be completed in the conditions of different test angles and loading forces.

The corresponding parameter values are obtained by the method of the nonlinear parameter fitting. Then the characteristics of tire lateral force with the change of sideslip angle and vertical load can be acquired. Figure 4 shows the relationship of tire lateral force and the sideslip angle under the condition of the load of 40KN, 50KN, 60KN. It can be seen that the fitting curves and test data coincide with each other very well. Then the lateral force can be obtained with the sideslip angle, vertical load and these fitting parameters. Figure 5 shows the tire cornering properties with the sideslip angle (0° – 10°) and vertical load (20KN-80KN) by the fitting parameters.

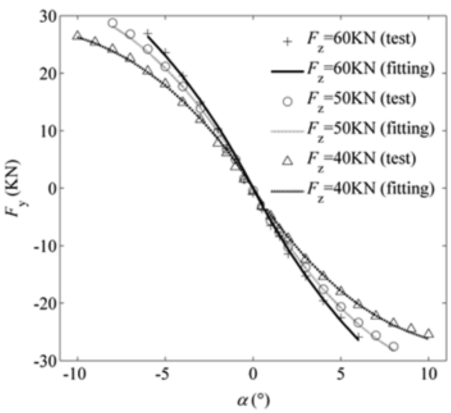

Figure 4. Tire lateral force with the change of sideslip angle.

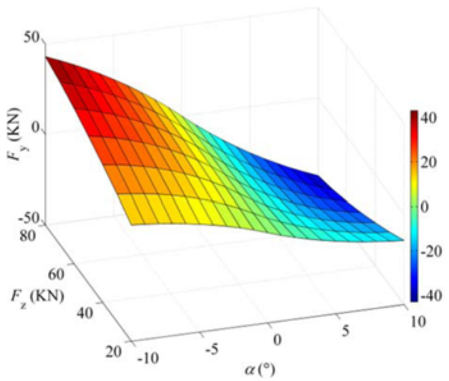

Figure 5. Tire lateral force with the change of sideslip angle and vertical load.

2.4. Steering Model

Generally speaking, multi-axle vehicles have different steering modes at different speeds. Just like the target vehicle in this paper, when the vehicle drives on the road at a certain speed, different steering modes (some shafts are locked in different degrees) appear. Since axle 1 and 2 are connected by mechanical means, axle 2 won't be locked in any case. However, axle 3, 4, 5 and 6 are electronically controlled by hydraulic steering system. This implies that different relationships exist between axle 2, 3, 4, 5, 6 and axle 1 when the vehicle is at different speeds, and they are shown as follows:

$$\delta_2 = a\tan\left(\left|\frac{X_2+\Delta}{X_1+\Delta}\right|\tan\delta_1\right) \tag{32}$$

$$\delta_3 = \begin{cases} a\tan\left(\left|\frac{X_3+\Delta}{X_1+\Delta}\right|\tan\delta_1\right) & (0 \le u \le 10\ \text{km/h}) \\ \left(1-\frac{u-10}{20}\right)a\tan\left(\left|\frac{X_3+\Delta}{X_1+\Delta}\right|\tan\delta_1\right) & (10\ \text{km/h} < u < 30\ \text{km/h}) \\ 0 & (u \ge 30\ \text{km/h}) \end{cases} \tag{33}$$

$$\delta_4 = \begin{cases} a\tan\left(\left|\frac{X_4+\Delta}{X_1+\Delta}\right|\tan\delta_1\right) & (0 \le u \le 10\ \text{km/h}) \\ \left(1-\frac{u-10}{20}\right)a\tan\left(\left|\frac{X_4+\Delta}{X_1+\Delta}\right|\tan\delta_1\right) & (10\ \text{km/h} < u < 30\ \text{km/h}) \\ 0 & (u \ge 30\ \text{km/h}) \end{cases} \tag{34}$$

$$\delta_5 = \begin{cases} a\tan\left(\left|\frac{X_5+\Delta}{X_1+\Delta}\right|\tan\delta_1\right) & (0 \le u \le 40\ \text{km/h}) \\ \left(1-\frac{u-10}{20}\right)a\tan\left(\left|\frac{X_5+\Delta}{X_1+\Delta}\right|\tan\delta_1\right) & (40\ \text{km/h} < u < 60\ \text{km/h}) \\ 0 & (u \ge 60\ \text{km/h}) \end{cases} \tag{35}$$

$$\delta_6 = \begin{cases} a\tan\left(\left|\frac{X_6+\Delta}{X_1+\Delta}\right|\tan\delta_1\right) & (0 \le u \le 40\ \text{km/h}) \\ \left(1-\frac{u-10}{20}\right)a\tan\left(\left|\frac{X_6+\Delta}{X_1+\Delta}\right|\tan\delta_1\right) & (40\ \text{km/h} < u < 60\ \text{km/h}) \\ 0 & (u \ge 60\ \text{km/h}) \end{cases} \tag{36}$$

2.5. Dynamic Toe Angle

A considerable number of studies have indicated that the toe angle has a great impact on tire wear. So the K&C (kinematics and compliance) characteristic experiment is conducted to get the characteristics of dynamic toe angle of each tire. The test vehicle is a six-axle steering heavy duty crane and the toe angles are affected by the lateral force most. As an example, Figure 6 shows the experimental data

Table 2. Toe angle with the change of lateral force.

Toe angle	Expression γ/(°)
Axle 1 (L)	$\gamma_{1L} = 1.458 \times 10^{-5}F_{Y1L} + 0.208$
Axle 1 (R)	$\gamma_{1R} = 1.933 \times 10^{-5}F_{Y1R} + 0.208$
Axle 2 (L)	$\gamma_{2L} = -1.541 \times 10^{-5}F_{Y2L} - 0.259$
Axle 2 (R)	$\gamma_{2R} = -1.041 \times 10^{-5}F_{Y2R} - 0.259$
Axle 3 (L)	$\gamma_{3L} = -1.129 \times 10^{-5}F_{Y3L} - 0.126$
Axle 3 (R)	$\gamma_{3R} = -0.963 \times 10^{-5}F_{Y3R} - 0.126$
Axle 4 (L)	$\gamma_{4L} = 1.652 \times 10^{-5}F_{Y4L} - 0.226$
Axle 4 (R)	$\gamma_{4R} = 2.443 \times 10^{-5}F_{Y4R} - 0.226$
Axle 5 (L)	$\gamma_{5L} = 0.871 \times 10^{-5}F_{Y5L} + 0.209$
Axle 5 (R)	$\gamma_{5R} = 1.382 \times 10^{-5}F_{Y5R} + 0.209$
Axle 6 (L)	$\gamma_{6L} = -1.045 \times 10^{-5}F_{Y6L} + 0.302$
Axle 6 (R)	$\gamma_{6R} = 0.687 \times 10^{-5}F_{Y6R} + 0.302$

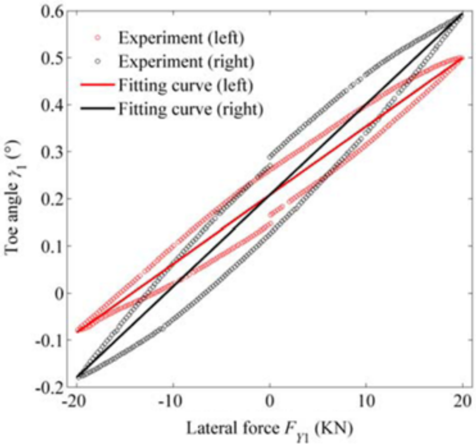

Figure 6. Toe angle of axle 1 with the change of lateral force.

and fitting curves of the toe angle of axle 1 with the change of lateral force. All the fitting relationships of these tires are shown in Table 2.

2.6. Test Verification of the Vehicle Model

The target vehicle is a six-axle steering heavy duty crane and the parameters of this vehicle are present in nomenclature part. The vehicle model verification test was performed in this part. In the experiment, the steering angle of axle 1, the vehicle speed, the lateral velocity, the yaw angle velocity and the roll angle velocity were measured.

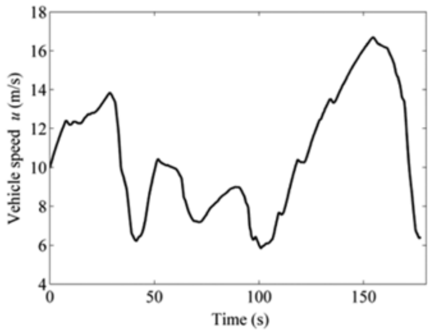

(a) Vehicle velocity

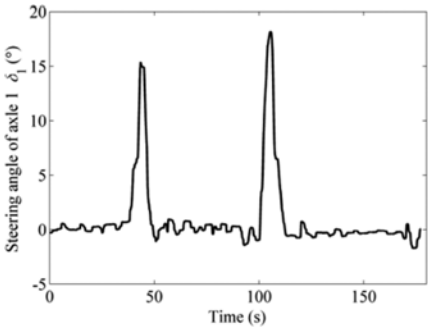

(b) Steering angle of axle 1

Figure 7. Object vehicle.

The specific approach is as following: let the vehicle drive on the road normally, and then made two trapezoidal steering test. The whole process was manipulated by the driver, so the trapezoidal steering test was not standard, and the control of the vehicle speed was not stable. These problems would make the test not very standard. In order to eliminate such effects, the signals of vehicle speed and the steering angle of axle 1, which is measured during the test, are used as the input in the simulation analysis.

As shown in Figures 7 (a) and (b), they are the curves of real vehicle velocity and steering angle of axle 1. The

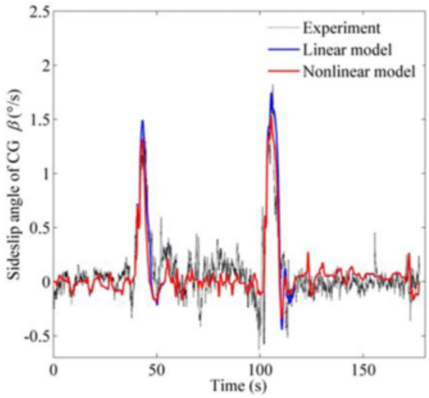

(a) Lateral velocity

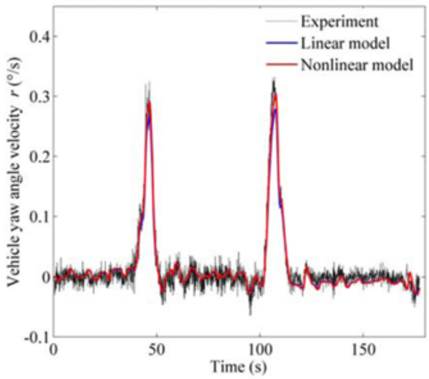

(b) Yaw angle velocity

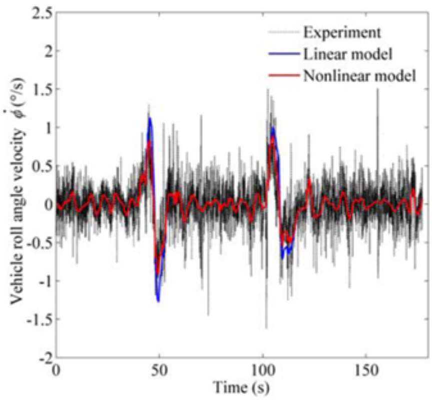

(c) Roll angle velocity

Figure 8. Object vehicle.

curves of real vehicle velocity and the steering angle of axle 1 were used as the signals of simulation input.

Figures 8 (a) ~ (c) are the sideslip angle of CG, yaw angle velocity and roll angle velocity curves of the vehicle separately. The dotted lines in the three figures are the test curves. Due to the interference of the outside and the precision of the equipment, the test curves have some noises, but the simulation curves are smooth relatively. It can be seen from the three figures that: the curves of the linear model and nonlinear model all coincide with the data of an experiment in a tolerant error range. But it is obvious that the curves of nonlinear model consistent with the test data better than that of a linear model in peak position especially. There are two main reasons: ① As Equation (19) shown, there are some nonlinear terms in the nonlinear dynamic model which are usually ignored in the linear dynamic model; ② In this paper, the characteristics of hydro-pneumatic suspension, tire, steering system and toe angle are considered, and these characteristics are obtained by the test. So the nonlinear model is more realistic, and it can be used to calculate the amount of tire wear more precisely.

3. TREAD WEAR MODEL AND TEST

Some algorithms of tire wear have already been proposed. In Miller *et al*. (1991), tire wear amount was considered to be proportional to the square to biquadrate of the sideslip angle. Qin (2011) utilized the concept of "ratio power of cornering wear" to calculate tire wear amount. In order to obtain the accurate wear amount by simulation, the local wear model based on "wear power" was adopted in this paper (Lupker *et al*., 2004):

$$R_{\mathrm{wear}} = aP_{\mathrm{f}}^{\mathrm{b}} \tag{37}$$

$$P_{\mathrm{f}} = \frac{F_{\mathrm{f}}\left|V_{\mathrm{s}}\right|}{A_{\mathrm{patch}}} \tag{38}$$

where, a and b are two fitting constants, different tires have different fitting values, the specific value of the constants can be obtained by fitting the test data. R_{wear} is wearing mass per unit time and unit area, P_{f} is wearing power per unit area, A_{patch} is contact area of friction, F_{f} is friction force, V_{s} is sliding speed of friction. In the vehicle dynamics, the tire friction force and sliding speed can be obtained by the following formulas:

$$\begin{cases} F_{\mathrm{f}} = F_{\mathrm{Yi}} \\ V_{\mathrm{s}} = u\tan\alpha_{\mathrm{i}} \approx u\alpha_{\mathrm{i}} \end{cases} \tag{39}$$

In order to acquire the fitting values of a and b, the local wear test was made in a wear test platform. The test platform mainly includes five parts are shown in Figure 9. The cement pavement and tread sample which are used for wear test are shown in Figure 10. The specific approach is as follows: the tread rubber sample is fixed on the measuring arm, the cement pavement which simulates the road face is fixed on the friction turntable, the servo motor drive system controls the sliding speed and the hydraulic system controls the vertical pressure. Meanwhile, the sliding speed and vertical pressure can be obtained by sensors.

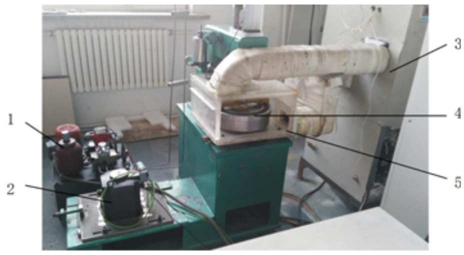

Figure 9. Wear test platform: 1. Hydraulic system; 2. Servo motor drive system; 3. Temperature control unit; 4. Friction turntable; 5. Environmental warehouse.

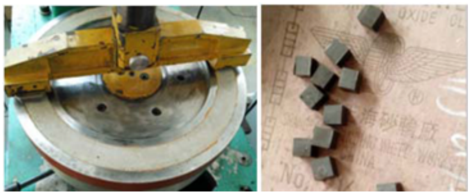

Figure 10. Cement pavement and tread sample.

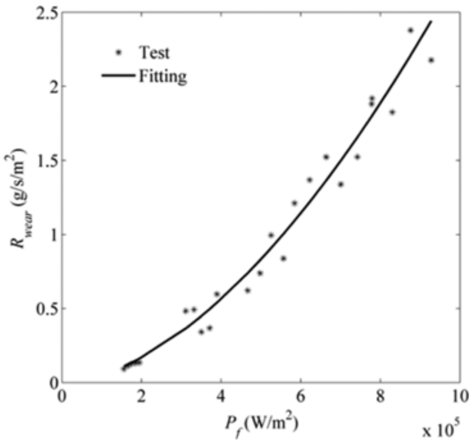

Figure 11. Wear characteristics of the tire tread.

By weighing the tread sample before and after wear test and measuring the data by the sensors mentioned above, the test data and fitting curves can be obtained and shown in Figure 11. The values of a and b can be fitted as: $a = 1.01 \times 10^{-10}$, $b = 1.74$, and the fitting precision reached 89.97 %.

4. TIRE WEAR AMOUNT

4.1. Calculation of the Wear Amount

Tire wear amount will occur inevitably when the vehicle is traveling on the road. There are many reasons for tire wear, in the case of the reasonable design of the vehicle, the tire wear caused by the lateral and longitudinal force are the main factors. For the complexity of longitudinal road conditions, the amount of tire wear caused by longitudinal force is very difficult to calculate. So the estimation method of the tire wear amount caused by lateral force is proposed only in this paper. According to Section 3, the tire wear height caused by the lateral force can be calculated by the following formulas after the vehicle running on the road for a period of time.

$$\begin{cases} \Delta h_{\mathrm{iL}} = \dfrac{\int_0^{\mathrm{T}} a\left[(F_{\mathrm{YiL}}(t)\cdot u(t)\cdot \alpha_{\mathrm{iL}}(t)/A_{\mathrm{patch\_iL}}\right]^{\mathrm{b}} A_{\mathrm{patch\_iL}}\,dt}{2\pi R_{\mathrm{iL}}\rho D_{\mathrm{patch}}} \\ \Delta h_{\mathrm{iR}} = \dfrac{\int_0^{\mathrm{T}} a\left[(F_{\mathrm{YiR}}(t)\cdot u(t)\cdot \alpha_{\mathrm{iR}}(t)/A_{\mathrm{patch\_iR}}\right]^{\mathrm{b}} A_{\mathrm{patch\_iR}}\,dt}{2\pi R_{\mathrm{iR}}\rho D_{\mathrm{patch}}} \end{cases} \tag{40}$$

$$\begin{cases} R_{\mathrm{iL}} = R_0 - F_{\mathrm{ziL}}/k_{\mathrm{z}} \\ R_{\mathrm{iR}} = R_0 - F_{\mathrm{ziR}}/k_{\mathrm{z}} \end{cases} \tag{41}$$

$$\begin{cases} A_{\mathrm{patch\_iL}} = 2\eta D_{\mathrm{patch}}\sqrt{R_0^2 - R_{\mathrm{iL}}^2} \\ A_{\mathrm{patch\_iR}} = 2\eta D_{\mathrm{patch}}\sqrt{R_0^2 - R_{\mathrm{iR}}^2} \end{cases} \tag{42}$$

where, R_0 is the free radius of the tire, R_{iL} and R_{iR} are the load radius of left and right tire of ith axle, respectively. ρ shows the rubber density of the tire tread, D_{patch} means the width of the tire grounding mark, $A_{\mathrm{patch\_iL}}$ and $A_{\mathrm{patch\_iR}}$ are the grounding area of left and right tire of ith axle, k_z represents the vertical stiffness of the tire, η is the proportion of the tire tread pattern area. Assume that the vehicle of turning left and right is almost the same probability, then the tire wear height of each axle can be expressed as:

$$\Delta h_{\mathrm{i}} = (\Delta h_{\mathrm{iL}} + \Delta h_{\mathrm{iR}})/2 \tag{43}$$

4.2. Road Information Collection

When the vehicle velocity and the steering angle of axle 1 are assigned, the tire wear amount can be calculated by these equations presented above. So it is necessary to test the vehicle velocity and steering angle of axle 1 accurately

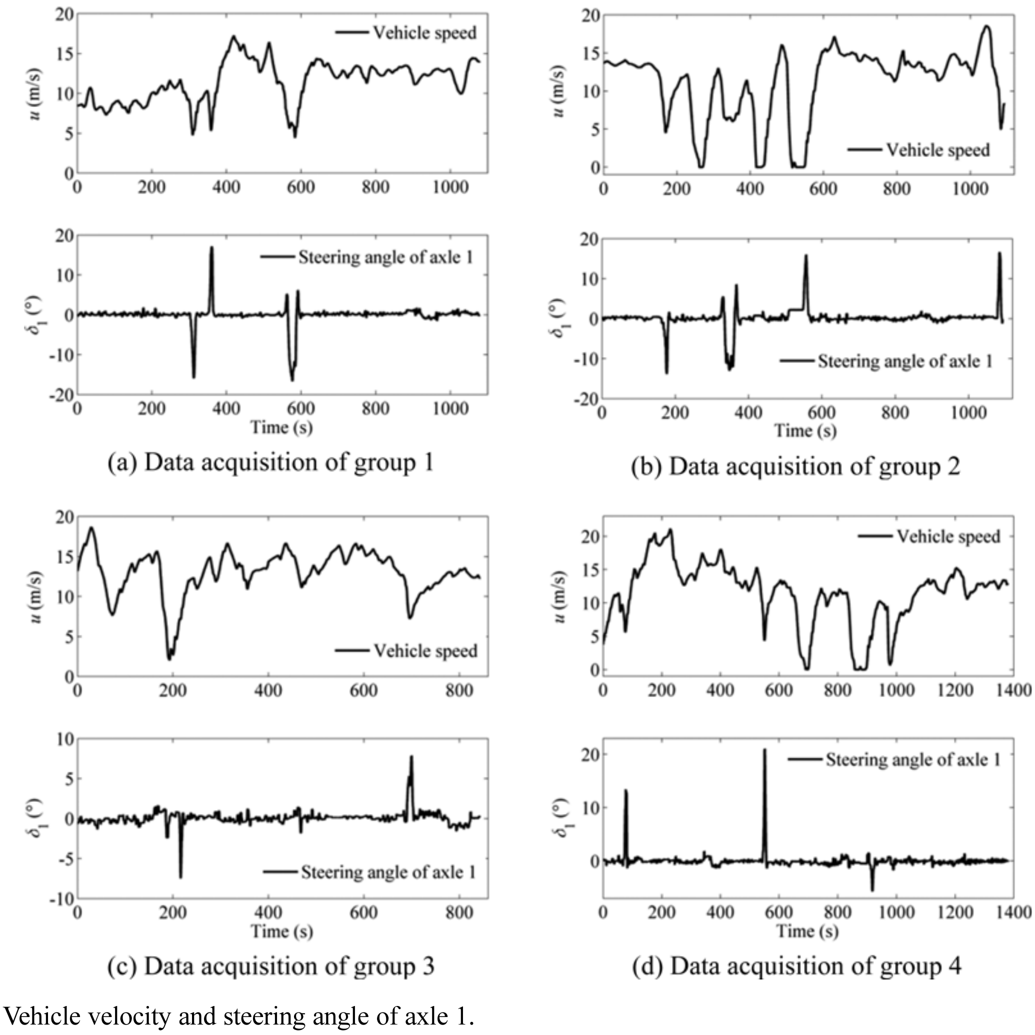

(a) Data acquisition of group 1

(b) Data acquisition of group 2

(c) Data acquisition of group 3

(d) Data acquisition of group 4

Figure 12. Vehicle velocity and steering angle of axle 1.

throughout the whole running process if the tire wear for a long distance is intended to be estimated. However, it will be difficult to estimate the amount of tire wear by this way. Therefore, the test of a short sample distance is used to take the place of a long distance, then the tire wear amount of a long distance can be estimated by amplifying the sample to an appropriate proportion (Huang *et al.*, 2013). In order to get the real road samples, four groups of real road information are collected in the long way process. Then the sample data of the velocity and the steering angle of axle 1 are used as the input signals of simulation to estimate the tire wear of long distance. Figures 12 (a) ~ (d) are the four groups of real road samples.

5. EXPERIMENT AND SIMULATION

In order to do an in-depth research work for the tire wear, a 5000 km road wear test was made in this paper. In the course of the experiment, 20 measuring points were distributed into five rows around the tire uniformly. And the height of the 20 points were measured before and after the wear test, then the average tire wear amount of every axle of the vehicle which had ran 5000 km can be obtained by the method of difference and average.

The total mileages of the four information groups mentioned in Section 4.2 are 54.72 km. So, in order to verify the effectiveness of the simulation algorithm, the distance of the four groups for simulation should be enlarged to 5000 km linearly. After the scaling, the tire wear amount of experiment and simulation for 5000 km can be obtained.

The wear amount of simulation is divided into two cases. They are the results calculated by a linear model and a nonlinear model. As shown in Figure 13, the bar of the experiment is the total wear amount, the bars of simulation of the linear model and nonlinear model is the wear amount caused by lateral dynamic only. From the compared illustration, it is obvious that: ① The value and the trend of simulation results reflect the real wear condition; ② The wear amount caused by lateral force occupies a considerable proportion of the total wear amount and the wear amount at the front and rear axle is more than that at the middle axle; ③ The wear amount calculated by nonlinear model is about 15 % larger than the linear model except axle 3.

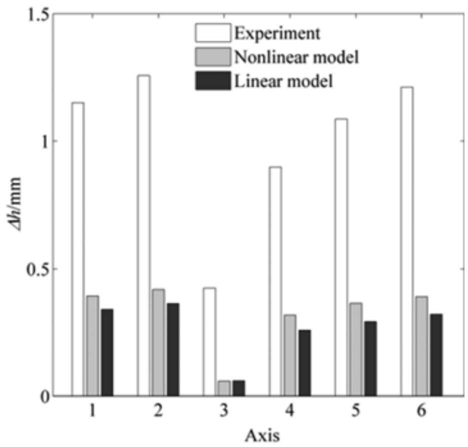

Figure 13. Comparison of experiment and simulation of tire wear of each axle.

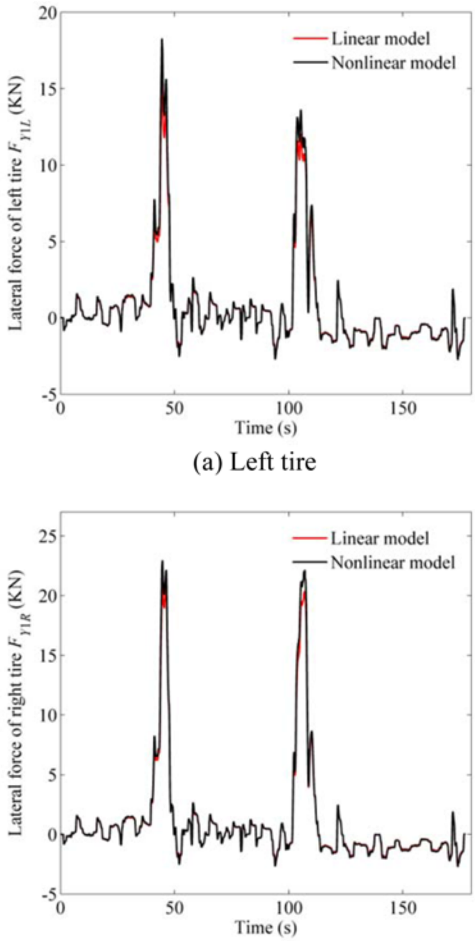

(a) Left tire

(b) Right tire

Figure 14. Sideslip angle of axle 1.

The wear amount is mainly caused by the sideslip angle, lateral force and grounding area of the tire from Equations (40) and (41). While, differences of the three factors exist in the linear model and nonlinear model, and the sideslip angle of the left and right tire of axle 1 which are shown in Figure 14 are given out as an example to explain the differences. The difference and accuracy of the two models are analyzed in Section 2.6. So the wear amount calculated by the nonlinear model is more authenticity.

As mentioned in many research, the toe angle has a significant influence on tire wear. In order to figure out how much the toe angle will affect tire wear, a deeper research about toe angle was performed. The amount of tire wear with different values of the initial toe angle was

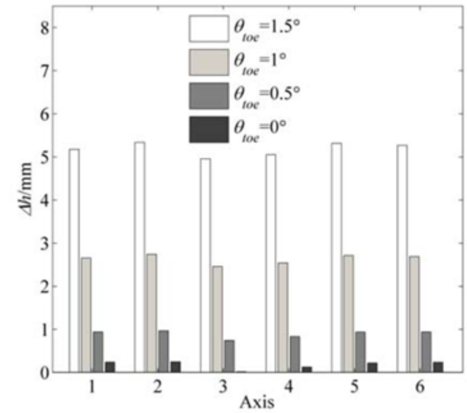

Figure 15. Tire wear amount with different toe angle.

calculated by simulation. As shown in Figure 15, the initial toe angle was assigned the value of 0°, 0.5°, 1°, 1.5° respectively, and the amount of tire wear is obtained and presented correspondingly. From this figure, it can be concluded that: ① The influence of the toe angle on tire wear is very large, ② It will occur abnormal tire wear if the toe angle is too big or the design is unreasonable, and the wear amount caused by lateral force will be the main influencing factors.

6. CONCLUSION

(1) A general mathematical nonlinear model with 3DOF was established for a multi-axle steering vehicle. This vehicle model is able to accurately describe the dynamics of hydro-pneumatic suspension, tire, steering system and toe angle. By comparing with the experimental results, the simulation results show that the vehicle model is more accurate and thus the vehicle parameters calculated by the nonlinear model are more precise.
(2) The experiment of rubber block wear was conducted and the fitting parameters of the "wear power" model were obtained. In order to obtain the real road condition, four sets of actual road data of the vehicle velocity and the steering angle of axle 1 were collected as the input signals for simulation analysis.
(3) The tire wear issue was analyzed quantitatively. By comparing the wear amount from both experiment and simulation, it demonstrated that the method proposed in this paper can be used to estimate the tire wear amount caused by lateral force. And the importance of the realistic nonlinear model in tire wear calculation is further illustrated.
(4) The research for tire wear affected by toe angle was done by simulation. The analysis can reflect that the abnormal wear may occur if the toe angle is too large or unreasonable, and the tire wear amount may be 3-10 times larger than that caused by normal wear when the toe angle increases to 1° – 1.5° (an unreasonable angle region).

ACKNOWLEDGEMENT–This research was supported by National Natural Science Foundation of China (Grant No. 51405185), China Postdoctoral Science Foundation (Grant Nos. 2015M581399, 2016T90250), China Automobile Industry Innovation and Development Joint Fund (Grant No. U1664257).

REFERENCES

Cho, J. C. and Jung, B. C. (2007). Prediction of tread pattern wear by an explicit finite element model. *Tire Science and Technology* **35**, **4**, 276–299.

Cho, J. R., Choi, J. H. and Kim, Y. S. (2011). Abrasive wear amount estimate for 3D patterned tire utilizing frictional dynamic rolling analysis. *Tribology International* **44**, **7-8**, 850–858.

Cho, J. R., Shin, S. W. and Yoo, W. S. (2005). Crown shape optimization for enhancing tire wear performance by ANN. *Computers & Structures* **83**, **12-13**, 920–933.

Da Silva, M. M., Cunha, R. H. and Neto, A. C. (2012). A simplified model for evaluating tire wear during conceptual design. *Int. J. Automotive Technology* **13**, **6**, 915–922.

Grosch, K. A. (2008). Rubber abrasion and tire wear. *Rubber Chemistry and Technology* **81**, **3**, 470–505.

Guo, K. H. (2011). *Theory of Vehicle Handling Dynamics*. Phoenix Science Press. Jiangsu, China.

Huang, H. B., Chiu, Y. J. and Jin, X. X. (2013). Numerical calculation of irregular tire wear caused by tread self-excited vibration and sensitivity analysis. *J. Mechanical Science and Technology* **27**, **7**, 1923–1931.

Klüppel, M. (2015). Wear and abrasion of tires. *Encyclopedia of Polymeric Nanomaterials*, **2015**, 2600–2604.

Knisley, S. (2002). A correlation between rolling tire contact friction energy and indoor tread wear. *Tire Science and Technology* **30**, **2**, 83–99.

Li, H. P., Shi, B. Q. and Zhang, W. M. (2006). Optimal design of heavy modular multi-axle trailer's steering mechanism. *Lifting the Transport Machinery* **2006**, **8**, 38–41.

Li, Y., Zuo, S., Lei, L., Yang, X. and Wu, X. (2012). Analysis of impact factors of tire wear. *J. Vibration and Control* **18**, **6**, 833–840.

Lupker, H., Cheli, F., Braghin, F., Gelosa, E. and Keckman, A. (2004). Numerical Prediction of car tire wear. *Tire Science and Technology* **32**, **3**, 164–186.

Ma, L. F., Wang, J., Xu, L. F. and Ouyang, M. G. (2015). Optimized torque distribution strategy for in-wheel-drive electric vehicles to reduce tire wear. *Vehicle Power and Propulsion Conf.* (*VPPC*), 1–5.

Miller, G., Reed, R. and Wheeler, F. (1991). Optimum Ackerman for improved steering axle tire wear on trucks. *SAE Paper No*. 912693.

Qin, G. (2011). *Research on Complex Mechanical System Modeling and Its Application in Multi-axle Chassis Development*. Ph. D. Dissertation. Huazhong University of Science & Technology. Wuhan, China.

Rodríguez-Tembleque, L., Abascal, R. and Aliabadi, M. H. (2010). A boundary element formulation for wear modeling on 3D contact and rolling-contact problems. *Int. J. Solids and Structures* **47**, **18-19**, 2600–2612.

Rodríguez-Tembleque, L., Abascal, R. and Aliabadi, M. H. (2011). A boundary elements formulation for 3D fretting-wear problems. *Engineering Analysis with Boundary Elements* **35**, **7**, 935–943.

Sakai, H. (1996). Friction and wear of tire tread rubber. *Tire Science and Technology* **24**, **3**, 252–275.

Shen, Y. H., Gao, Y. and Xu, T. (2016). Multi-axle vehicle dynamics stability control algorithm with all independent drive wheel. *Int. J. Automotive Technology* **17**, **5**, 795–805.

Stalnaker, D. O. and Turner, J. L. (2002). Vehicle and course characterization process for indoor tire wear simulation. *Tire Science and Technology* **30**, **2**, 100–121.

Stalnaker, D., Turner, J., Parekh, D., Whittle, B. and Norton, R. (1996). Indoor simulation of tire wear: Some case studies. *Tire Science and Technology* **24**, **2**, 94–118.

Xu, N. (2012). *Study on the Steady State Tire Model under Combined Conditions*. Ph. D. Dissertation. Jilin University. Changchun, China.

Yang, J., Wang, G. L., Wan, Z. J., Liang, C. and Zhou, H. C. (2016). Non-natural equilibrium contour design for radial tire and its influence on tire performance. *Int. J. Automotive Technology* **17**, **4**, 639–649.

Yu, F. and Lin, Y. (2005). *Vehicle System Dynamics*. China Machine Press. Beijing, China.

Zhu, Y. F., Ding, H. G., Zhang, X. J. and Li, X. (2015). Tire cornering wear control of multi-axle vehicle. *Machinery Design and Manufacture* **09**, **295**, 85–88.

Zhuang, J. D. (2002). *Advanced Technology of Tire*. Beijing Science and Technology Press. Beijing, China.

Zuo, S. G., Ni, T. X., Wu, X. D., Wu, K. and Yang, X. W. (2014). Prediction rocedure for wear distribution of transient rolling tire. *Int. J. Automotive Technology* **15**, **3**, 505–515.